minerals

MDPI

Article

Geological Characteristics and Genesis of the Greisen-Hosted Nb-Ta Mineralization in the Qidashan Iron Deposit, Liaoning Province, China, and Its Implications

Yang Xiao [1], Rongzhen Gao [1,*], Qing Sun [2,3], Jianfei Fu [1], Yuzeng Yao [1], Sanshi Jia [1,4] and Jiale Chen [1]

[1] Department of Geology, College of Resources and Civil Engineering, Northeastern University, Shenyang 110819, China; xiaoyang1374@163.com (Y.X.); yaoyuzeng@mail.neu.edu.cn (Y.Y.); jiasanshi@neuq.edu.cn (S.J.)
[2] Baotou Rare Earth Research Institute, Baotou 014000, China; sq4132113@163.com
[3] National Kev Laboratory of Banunobo Rare Earth Resource Researches and Comorehensive Utilization, Baotou 014000, China
[4] School of Resource and Materials, Northeastern University at Qinhuangdao, Qinhuangdao 066004, China
* Correspondence: gaorongzhen@mail.neu.edu.cn; Tel.: +86-153-929-42906

Abstract

The newly identified greisen-hosted Nb-Ta mineralization in the Qidashan iron deposit, Liaoning Province, China, offers a unique opportunity to explore how hydrothermal processes contribute to the enrichment of critical metals. In this study, an integrated analytical approach of petrographic observation and scanning electron microscopy–energy-dispersive spectrometer (SEM-EDS), electron probe microanalyzer (EPMA), and laser ablation inductively coupled plasma mass spectrometer (LA-ICP-MS) U-Pb dating of columbite-group minerals (CGMs) were employed to systematically decipher the paragenetic sequence, micro-structure, elemental composition and mineralization age of CGMs, aiming at the genesis of greisen-hosted Nb-Ta mineralization. The mineralization is characterized by the abundant occurrence of CGMs. Three generations of CGMs and two mineralization stages are distinguished: stage I contains CGM Is and CGM IIs, with Nb_2O_5 ranging from 25.7 to 69.56 wt.% and Ta_2O_5 from 5.8 to 52.5 wt.%; stage II contains CGM IIIs, with Nb_2O_5 between 59.5 and 71.5 wt.% and Ta_2O_5 between 3.5 and 16.2 wt.%. CGM Is consist of euhedral, homogeneous crystals of more than 100 μm, exhibit low Ta/(Nb + Ta) ratios (0.05–0.06) and high Mn/(Fe + Mn) ratios (0.19–0.26), and belong to columbite-Fe. CGM IIs generally overgrow on CGM Is with hydrothermal overprinting textures, and show significant compositional gaps compared to CGM Is, exhibiting higher Ta/(Nb + Ta) ratios (0.13–0.55) and restricted Mn/(Fe + Mn) ratios (0.15–0.18), with some belonging to columbite-Fe and others to tantalite-Fe, which reveals a transition from magma to "hydrosilicate fluid". CGM IIIs are mainly anhedral and homogeneous, with a grain size of less than 50 μm. However, some CGM IIIs overgrow on CGM IIs and/or CGM Is with patchy textures indicative of subsequent hydrothermal overprinting of hydrosilicate fluid, forming a coarse-grain size over 100 μm. CGM IIIs are characterized by lower Ta/(Nb + Ta) ratios (0.03–0.14) and variable Mn/(Fe + Mn) ratios (0.08–0.26), and they belong to columbite-Fe. LA-ICP-MS U-Pb dating yields weighted mean $^{206}Pb/^{238}U$ ages of 2646 ± 15 Ma for stage I and 2500 ± 28 Ma for stage II, indicating two-stage Nb-Ta mineralization. The early mineralization may correlate with the partial melting of volcanic–sedimentary rocks due to the geothermal anomalies associated with ~2.7 Ga submarine volcanism, and the late mineralization formed by the magmatic hydrothermal activities related to emplacement of the Qidashan granite in 2.5 Ga. We therefore propose that the two-stage greisen-hosted Nb-Ta mineralization probably widely occurred in these sedimentary–metamorphic iron deposits in the Anshan–Benxi area and even in the northern edge of the North China Craton, and it may provide new insights for evaluating the Nb-Ta resource potential in similar Algoma-type iron deposits globally.

Check for updates

Academic Editor: Pura Alfonso

Received: 29 January 2026
Revised: 9 March 2026
Accepted: 13 March 2026
Published: 16 March 2026

Copyright: © 2026 by the authors. Licensee MDPI, Basel, Switzerland. This article is an open access article distributed under the terms and conditions of the Creative Commons Attribution (CC BY) license.

Keywords: Qidashan; columbite-group minerals; greisen-hosted Nb-Ta mineralization; hydrosilicate fluid; Algoma-type iron deposits

1. Introduction

Niobium (Nb) and tantalum (Ta) are widely used in emerging and electronic industries due to their unique physical and chemical properties, and they have become strategic critical resources underpinning cutting-edge technologies [1–3]. Nb-Ta mineralization is typically linked to a combination of magmatic and hydrothermal processes. The compositional variations observed in Nb-Ta-bearing minerals are used to identify magmatic fractional crystallization [2,4–6], while the textures resulting from replacement are primarily a sign of hydrothermal alteration [6–8]. A significant debate exists regarding which of these mechanisms plays a more dominant role in the mineralization [9–15]. LA-ICP-MS U-Pb dating of columbite-group minerals is frequently employed to determine the age of mineralization. However, the current laser beam diameter used, generally ranging from 45 to 90 μm, is too broad, hindering accurate micro-scale U-Pb dating of smaller grains or those with complex textures. A newly introduced high-resolution LA-ICP-MS method overcomes this challenge by utilizing specific standards for CGMs based on their Ta/(Nb + Ta) and Mn/(Fe + Mn) ratios, which helps to correct for matrix effects linked to the smaller beam size [16], thus allowing for precise dating of Nb-Ta mineralization of fine-grained CGMs and coarse-grained CGMs with complex textures.

Nb-Ta ore deposits around the world are predominantly hosted in highly fractionated and evolved granites and granitic pegmatites, as well as in some alkaline rocks and carbonatites [17–19]. However, greisen-hosted Nb-Ta mineralization has recently been reported at the Qidashan iron deposit in Liaoning Province, China [20], which is spatially closely associated with high-grade iron ore bodies. Greisen is traditionally recognized as a common hydrothermal alteration of wall rocks adjacent to mineralized granite bodies [21–25], involving the granitic magmatism and subsequent magmatic–hydrothermal processes [26–28]. Previous studies have revealed that the greisen at the Qidashan iron deposit was predominantly formed through the autometasomatism of the Qidashan granite [29].

In this study, detailed geological characteristics and geochemical compositions of the greisen-hosted Nb-Ta mineralization within the Qidashan iron deposit were integrated using a suite of advanced analytical techniques, including scanning electron microscopy–energy-dispersive spectrometer (SEM-EDS), electron probe microanalyzer (EPMA), and laser ablation inductively coupled plasma mass spectrometer (LA-ICP-MS) U-Pb dating, aiming to determine the micro-textures and chemical compositions of the Nb-Ta-bearing minerals, constrain the precise age of the Nb-Ta mineralization, and reveal the genesis of greisen-hosted Nb-Ta mineralization and iron ore formation. This study not only deepens the understanding of the altered rock-type Nb-Ta mineralization mechanism at Qidashan and the significance of the hydrothermal process, but it also provides a collaborative theoretical reference for the prospecting breakthrough of greisen-hosted Nb-Ta mineralization within the sedimentary–metamorphic iron deposits in the Anshan–Benxi area and even in the northern edge of the North China Craton, as well as in other clustering terrains of Algoma-type iron deposits worldwide.

2. Geological Setting

2.1. Regional Geology

The Qidashan iron deposit in the Anshan–Benxi area is located at the junction between the Longgang Block and the Jiao–Liao–Ji belt (Figure 1a) in the northern segment of the Eastern Block of the North China Craton [30–32]. The area is predominantly characterized by exposed strata of the Neoarchean Anshan Group and the Lower Paleoproterozoic Liaohe Group

(Figure 1b) [31–33]. The Anshan Group can be divided into the Cigou, Dayugou, and Yingtaoyuan formations. The Cigou Formation consists mainly of amphibolite-facies metamorphic rocks, including mica schist, magnetite quartzite, plagioclase amphibolite, and hornblende plagiogneiss, and is a key host strata for sedimentary–metamorphic iron deposits in the region, such as the Gongchangling and Nanfen iron deposits [34,35]. The Dayugou Formation is predominantly composed of an amphibolite-facies metamorphic volcanic–sedimentary sequence of leptynite, leucoleptite, gneiss, and quartz schist, with some plagioclase amphibolite and magnetite quartzite at the lower part. It is similar to the Cigou Formation in metamorphic grade; however, only minor sedimentary–metamorphic iron deposits such as Xiaoyanggou are hosted in the Dayugou Formation. The Yingtaoyuan Formation is primarily composed of chlorite schist, sericite–chlorite schist, sericite–chlorite–quartz schist, chlorite–quartz schist, and phyllite, intercalated with thick-bedded banded magnetite quartzite. This sequence represents a thick series of fine-grained clastic rocks with intermediate-acid volcaniclastic intercalations. It has undergone greenschist-facies metamorphism [34,36,37], which is equivalent to the upper sedimentary sequence of a greenstone belt. The Liaohe Group represents an Early Proterozoic paleo-rift sequence that has undergone regional greenschist-facies metamorphism. The Langzishan and Lieryu formations are the predominantly exposed units of the Liaohe group in the study area [38]. The Liaohe Group unconformably overlies the Anshan Group, and the Quaternary sediments unconformably overlie the Anshan and Liaohe groups [33,39,40].

In the Anshan–Benxi area, granitic plutons are categorized into three distinct age groups: 3.1–3.8 Ga, 2.9–3.0 Ga, and 2.5 Ga (Figure 1b). The plutons of 3.1 to 3.8 Ga are mainly exposed in the southwestern part of Qidashan, including the ancient complex (older than 3.3 Ga), the Lishan granite (3140.6 ± 7.1 Ma) and the Chentaigou granite (3128 ± 6 Ma to 3360 ± 10 Ma) [41–43]. The granitic plutons of 2.9 to 3.0 Ga are generally located to the south of Qidashan, such as the Dong'anshan granite (3001 ± 4 Ma) and the Tiejiashan granite (2.95–3.0 Ga) [44,45]. The regional complex older than 3.3 Ga indicates the emergence of ancient continental nuclei, while the granites from 2.95 to 3.3 Ga signify the evolution of proto-continental blocks [43]. The exposed Qidashan granite to the east of Qidashan, which forms by recycling of mature old continental crust [46], yielding a weighted mean age of 2503 ± 10 Ma by LA-ICP-MS zircon U-Pb dating [47], may represent a stage of regional crustal stabilization [43].

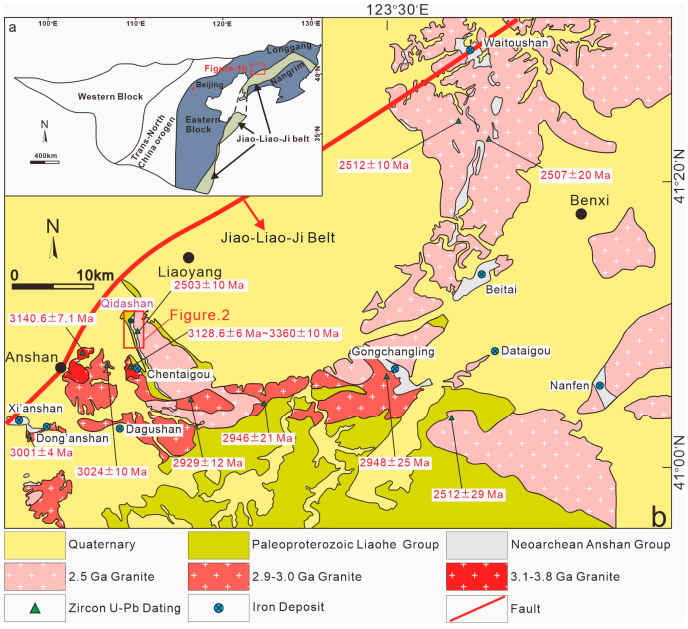


Figure 1. (**a**) Tectonic sketch of the North China Craton showing the location of the Anshan–Benxi area [48]. (**b**) Geological map of the Anshan–Benxi area showing the location of the Qidashan iron deposit. Green triangles indicate published zircon U-Pb ages for some pluton [47,49].

2.2. Deposit Geology

The Qidashan iron deposit has been mined since 1918, with proven iron ore reserves reaching 1.641 billion tons as of 2008 [50]. However, Li et al. first documented altered rock (including greisen and chlorite rock)-hosted Nb-Ta mineralization associated with high-grade iron ore within the deposit [20]. Samples collected from this zone yielded an average Nb-Ta grade of 0.019%, indicating significant exploration potential [20]. The outcrop strata in the Qidashan iron deposit mainly consist of the Yingtaoyuan Formation of the Neoarchean Anshan Group, the Langzishan Formation of the Lower Paleoproterozoic Liaohe Group, and the Quaternary. The iron ore bodies, including the low-grade banded iron formations (BIFs) and high-grade ore bodies, are all hosted in the Yingtaoyuan Formation. The well-developed faults can be divided into three groups according to their spatial relationship to the BIFs: the NNW-, NEE- and NNE-trending faults. The tensile tectonic affinity may be beneficial to the circulation of hydrothermal fluids and the formation of high-grade iron ore bodies [29], as these iron ore bodies are generally confined in the intersecting segments of NW- and NEE-trending faults. The BIF appears as a thick, steeply inclined tabular mass that aligns with the surrounding strata. It stretches over 5000 m, with a thickness ranging from 170 to 250 m, striking NW and dipping between 75° and 90° towards the SW. Zircon U-Pb dating of the Qidashan biotite–sericite–quartz schist yields a dominant age population of 2.56–2.53 Ga, interpreted as the timing of BIF deposition, with a minor age of ~2.7 Ga from magmatic zircon, which may record an earlier episode of BIF formation, likely associated with periodic large-scale submarine hydrothermal exhalation [51]. Furthermore, the high-grade iron ore bodies generally share the same orientation as the BIF (Figure 2b). These ore bodies are 10 to 150 m in length, are 2 to 50 m in thickness, and can reach depths of 40 to 450 m. The formation of these high-grade ore bodies was considered to be associated with the Qidashan granitic pluton and its subsequent magmatic hydrothermal fluids, resulting in the iron enrichment at 2.5 Ga [29].

The Nb-Ta mineralization within the greisens and chlorites are characterized by columbite-group minerals (CGMs), which are spatially associated with high-grade iron ores (Figures 2c and 3a). The geological–geochemical profile indicates that the greisens are all Nb-Ta-mineralized, which can be divided into greisen and tourmaline greisen based on their mineral compositions, and tourmaline unevenly aggregate in the central zone of the greisen in the profile (Figure 3a). The tourmaline greisen can contain 75.9–140.0 ppm (with an average of 97.0 ppm) and 10.7–20.2 ppm Ta (averaging 15.1 ppm). And greisen is characterized by a similar Nb-Ta content to tourmaline greisen, including 73.4–118.5 ppm Nb (averaging 95.2 ppm) and 10.1–21.6 ppm Ta (averaging 16.0 ppm). However, Nb-Ta concentrations in greisens increase toward contact with high-grade iron ore (Figure 2c). The greisens in the periphery are grayish-white, and consist of fine-grained quartz, sericite (Figure 3b), and muscovite with an increasing trend in grain size from the periphery to the center. The central zones are characterized by coarse-grained quartz, sericite, muscovite and tourmaline (Figure 3c). The distribution of tourmaline aggregations always has a certain degree of orientation (Figure 3d), possibly indicating the structural deformation and hydrothermal activities. Locally, coarse-grained quartz fills the open space as veins in the central zone (Figure 3e). In the greisens, two different grain sizes of quartz were identified in both the periphery and center under a microscope. Fine-grained quartz is less than 50 μm, and is enclose by muscovite (Figure 4a). It is generally distributed around muscovite or coarse-grained quartz (Figure 4b). However, coarse-grained quartz is usually larger than 100 μm (Figure 4a,b). The contact interface between coarse-grained quartz and fine-grained quartz is not distinct (Figure 4b), suggesting that the coarse quartz may originate from the recrystallization of the fine-grained quartz. Tourmaline, typically over 100 μm in size, often forms clustered aggregates, and can be cross-cut by coarse-grained quartz (Figure 4c). In addition, tourmaline is surrounded by sericite with anhedral crystals (Figure 4d).

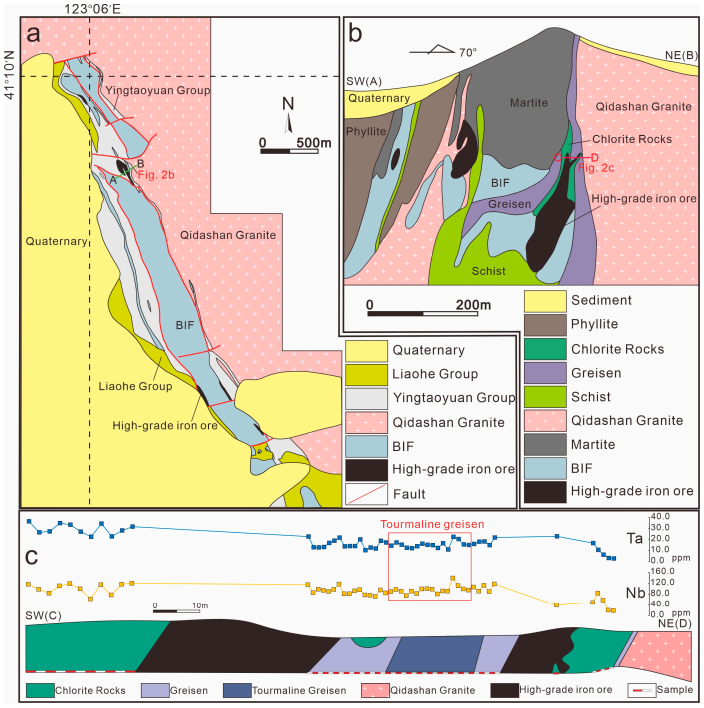


Figure 2. (**a**) Geological map of the Qidashan iron deposit showing the location of Profile A-B [29]. (**b**) Schematic diagram of Profile A-B showing the location of the geological–geochemical Profile C-D [29]. (**c**) Geological–geochemical profile of the Nb-Ta-mineralized greisen at Qidashan.

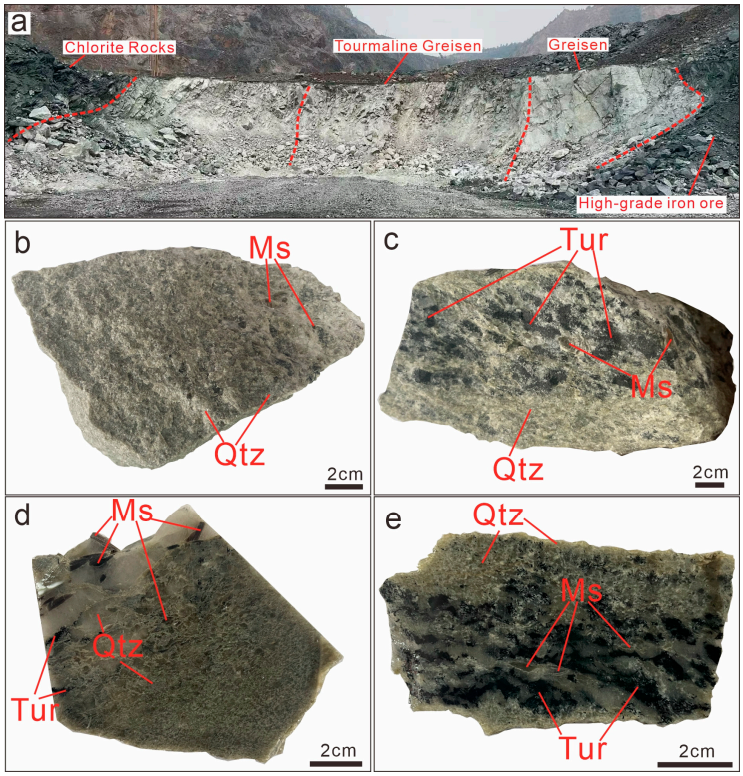


Figure 3. Photographs of outcrops and hand specimens of Nb-Ta-mineralized greisens from the Qidashan iron deposit. (**a**) Greisen is spatially associated with chlorites and high-grade iron ore bodies. The red dash lines represent the boundaries between different lithologies. (**b**) Greisen is fine-grained and is composed of sericite, muscovite and quartz in the periphery. (**c**) Tourmaline greisen exhibits a coarse grain and is composed of sericite, muscovite, quartz, and tourmaline in the central zone. (**d**) Tourmaline shows a strong degree of orientation. (**e**) Quartz veins cut through the greisen. Abbreviations: Ms—muscovite; Qtz—quartz; Tur—tourmaline.

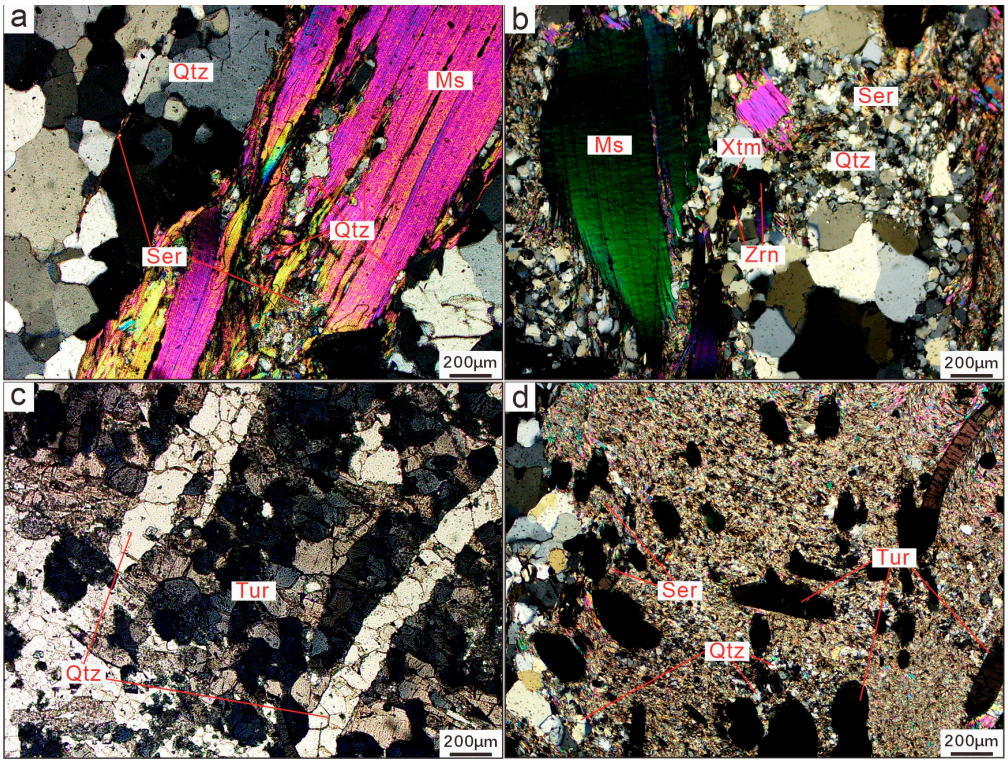


Figure 4. Microphotographs of thin sections of Nb-Ta-mineralized greisen in the Qidashan iron deposit. (**a**) Muscovite encloses fine-grained quartz and sericite. (**b**) The interface between coarse-grained quartz and fine-grained quartz is blurred. (**c**) Tourmaline cross-cut by coarse-grained quartz. (**d**) Tourmaline enclosed in sericite. Abbreviations: Ms—muscovite; Qtz—quartz; Ser—sericite; Tur—tourmaline; Xtm—xenotime; Zrn—zircon.

3. Samples and Analytical Methods

A total of 15 representative Nb-Ta-mineralized greisen samples were obtained from the geological–geochemical profile at the −210 m stage of the Qidashan open pit-. They were then prepared for polished thin sections. Based on petrographic and mineralogical observations under the microscope, the mineral assemblage of the Nb-Ta-mineralized greisens and the occurrence of the CGMs were investigated using scanning electron microscopy with energy-dispersive spectroscopy (SEM-EDS) and the automated mineralogy and chemical imaging system (AMICS). Representative CGM grains, particularly those exhibiting compositional zones and complex textures, were subsequently selected for a high-spatial electron probe microanalysis (EPMA) for major elements and LA-ICP-MS U-Pb dating for mineralization ages.

3.1. SEM-EDS

Scanning electron microscopy (SEM) and energy dispersion spectroscopy (EDS) were performed at the Test and Analysis Center of Northeastern University, Shenyang. The SEM instrument used was a Thermo Scientific Apreo 2C (Thermo Fisher Scientific Brno s.r.o., Brno, Czech Republic), and the operating conditions were as follows: 15 kV voltage, 10 nA beam current, −4 Epa vacuum degree, and 8.5 mm working distance. Before the experiment, the thin sections were electrically treated, and carbon spray treatment was selected to ensure that the spectrometer could identify Nb and Ta more effectively. The semi-quantitative chemical compositions of the selected minerals were determined by EDS (Oxford Ultim Max, Oxford Instruments, Abingdon, UK).

3.2. AMICS

The AMICS analysis was conducted at the State Key Laboratory of Rare Earth Resources Research and Comprehensive Utilization in Bayan Obo. The instrumentation consisted of a SIGMA 500 field emission scanning electron microscope (Carl Zeiss AG, Oberkochen, Germany) coupled with the AMICS software suite 2025 (comprising the four core programs: MAICSTool, MineralSTDManager, Investigator, and AMICSProcess). The analysis was performed under the following operational conditions: an accelerating voltage of 20 kV, a working distance of 8.5 mm, and a vacuum environment of −4 Epa.

3.3. EPMA

The quantitative analysis of in situ major elements of minerals was completed by using an electron probe microanalyzer from Wuhan SampleSolution Analytical Technology Co., Ltd., Wuhan, China. The analysis was completed using JXA-8230 of JEOL (JEOL Ltd., Akishima, Tokyo, Japan). The analyzed voltage and current were 15 KV and 20 nA. The standards used for calibration included niobium (NbLα), tantalum (TaMα), hematite (FeKα), rhodonite (MnKα), rutile (TiKα) and tungsten (WMa). The peak analysis time of the Ti, Fe, Mn, Nb, W and Ta elements was 10 s. The background analysis time was 5 s. The data correction method adopted the ZAF correction method of JEOL. Based on the counting statistics, the measurement error expressed as 2σ was approximately <1 rel.% for concentrations around 20 wt.%; <5 rel.% for concentrations around 5 wt.%; and <15 rel.% for concentrations around 1 wt.%.

3.4. LA-ICP-MS U-Pb Dating

The LA-ICP-MS U-Pb dating of CGM samples was carried out at CUGB Milma Lab, using a RESOlution S155 LR 193 nm ArF excimer laser ablation system coupled with a Thermo Fisher Neptune Plus LA-ICP-MS (Thermo Fisher Scientific, Bremen, Germany). The instrumental parameters, including the flow rate of Ar, N_2, and He, the inlet system, and the source parameters, were adjusted for a high signal sensitivity to obtain more precise and accurate data. Utilizing a 75 μm laser line scan ablation width under 3 J cm^{-2} energy fluence and 10 Hz repetition, Neptune Plus LA-ICP-MS demonstrated a standard sensitivity of 12 mV for ^{238}U on the NIST 614 (~880, 000 cps per mg U) in this study. The integration time was set up to 0.131 s. ^{202}Hg, $^{204}(Pb + Hg)$, ^{206}Pb, ^{207}Pb, ^{208}Pb, ^{232}Th, and ^{238}U were acquired simultaneously using different detector configurations: ^{202}Hg on IC4, $^{204}(Pb + Hg)$ on IC5, ^{206}Pb on IC2, ^{207}Pb on IC1B, ^{208}Pb on IC6, ^{232}Th on H3, and ^{238}Uon H4. The amplifiers H3 and H4 were configured with a resistance of 1011 Ω. In our study, we used a laser repetition of 5 Hz, an energy density of 3 J cm^{-2}, and a spot size of 15 μm. Each analytical sequence comprised two spot analyses each for the primary standards Coltan139 and CT1; secondary standards DKLS-27, CT3, and NP-2 [16]; and eight spot analyses of the samples. Moreover, each spot analysis consisted of pre-ablation of three cleaning shots and 20 s of background measurement followed by 30 s of ablation and 20 s of washout. The analyses were carried out during the 20 s background measurement with the laser switched off, 30–40 s ablation, and 20 s washout, where ^{202}Hg, ^{204}Pb, ^{206}Pb, ^{207}Pb, ^{208}Pb, ^{232}Th, and ^{238}U were measured during 10 ms, 20 ms, 20 ms, 30 ms, 15 ms, 10 ms, and 15 ms. The raw data were reduced offline using the software Iolite V4.8.4 [52]. We employed the "X_U_Pb Geochron 4" dynamic reduction scheme (DRS) within Iolite and Coltan139 as the external standard to correct the $^{206}Pb/^{238}U$, $^{207}Pb/^{235}U$, and $^{207}Pb/^{206}Pb$ ratios for all the reference standards and application samples [16]. A down-hole fractionation correction was applied in the Iolite software. Due to the low content of common Pb in CGMs, no common Pb correction was applied during the data processing. The final age calculations, weighted mean calculations, and concordia diagram construction were performed using Isoplot version 4.15.

4. Results

4.1. Petrography and Mineralogy of CGMs

The microscopy, AMICS, and EPMA all confirmed that CGMs are the exclusive Nb-Ta-bearing phase. Three generations of CGMs were distinguished, i.e., CGM Is, CGM IIs and CGM IIIs. CGM Is and CGM IIs were found enclosed by tourmaline (Figures 5a and 6). Zircon locally replaced the margins of CGM Is (Figure 5b), which exceeded 100 μm in size and showed a euhedral homogeneous structure and a low brightness in SEM (Figure 7a). CGM IIs typically overgrew on the rim of CGM Is, showing hydrothermal overprinting (Figure 7a). It was also found that CGM IIs completely pseudomorphously replaced CGM Is, preserving the original crystal forms and showing a higher brightness at rim than the core (Figure 7b).

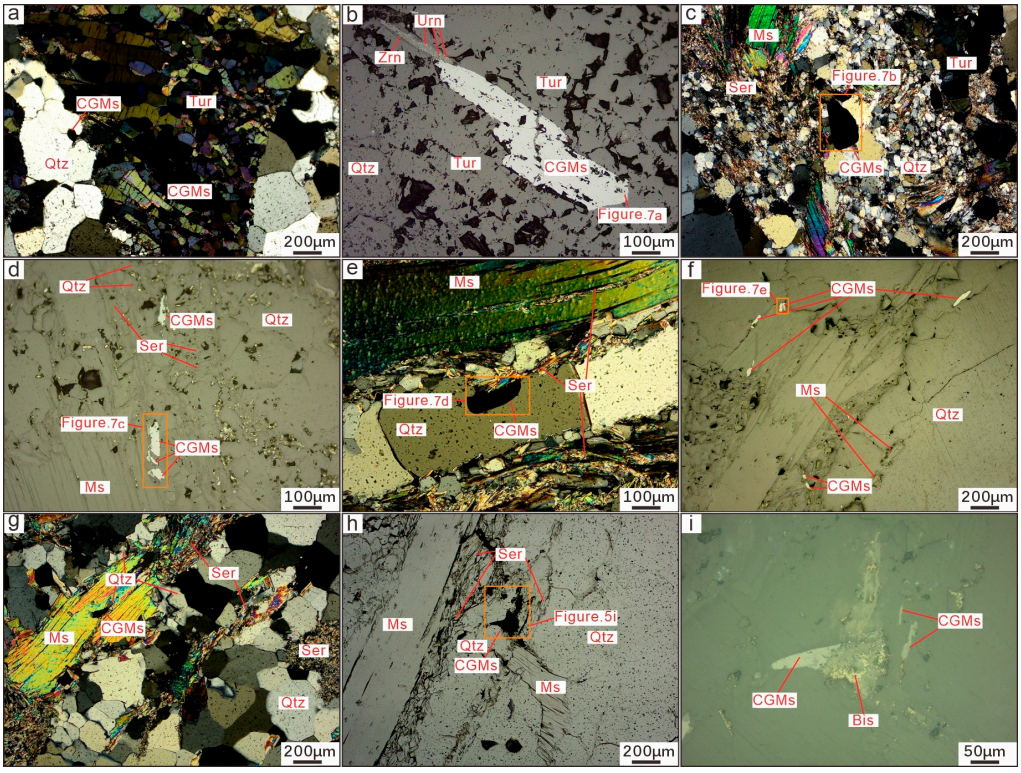


Figure 5. Microphotographs of GCMs in different generations within Nb-Ta-mineralized greisen at Qidashan. (**a**) Under plane-polarized light (PPL), CGM Is and CGM IIs are associated with tourmaline. (**b**) Under reflected light (RL-PPL), CGM Is are replaced by zircon. (**c**) Under cross-polarized light (XPL), CGM IIIs, which overgrow on CGM IIs, are associated with coarse-grained quartz and sericite. (**d**) Under RL-PPL, CGM IIIs are associated with muscovite. (**e**) Under XPL, CGM IIIs exhibit a replacement texture with muscovite. (**f**) Under RL-PPL, CGM IIIs are associated with coarse-grained quartz and muscovite. (**g**) Under XPL, CGM IIIs are enclosed within muscovite. (**h**) Under PPL, CGM IIIs show intense replacement, as evidenced by their anhedral morphology. (**i**) Under RL-PPL, CGM IIIIs are replaced by bismuthinite. Abbreviations: Bis—bismuth; CGMs—columbite-group minerals; Ms—muscovite; Qtz—quartz; Ser—sericite; Tur—tourmaline; Urn—uranium; Zrn—zircon.

CGM IIIs are typically found around quartz (Figure 5c) and muscovite (Figure 5d), enclosed by quartz (Figure 5e) or muscovite (Figure 5f,g). CGM IIIs are anhedral, less than 50 μm in size and always replaced by muscovite. Rarely, CGM IIIs are replaced by bismuthinite (Figure 5h,i). CGM IIIs typically show a low brightness in SEM, and the replacement fronts where CGM IIs pseudomorph muscovite commonly exhibit uranium enrichment (Figure 7c–e). However, CGM IIIs can overgrow on CGM IIs, showing a sharp relationship at the contact interface with larger sizes over 100 μm (Figure 7b). This is

characterized by faint oscillatory zoning and hydrothermal overprinting at the rim with a patchy texture inside (Figure 7b).

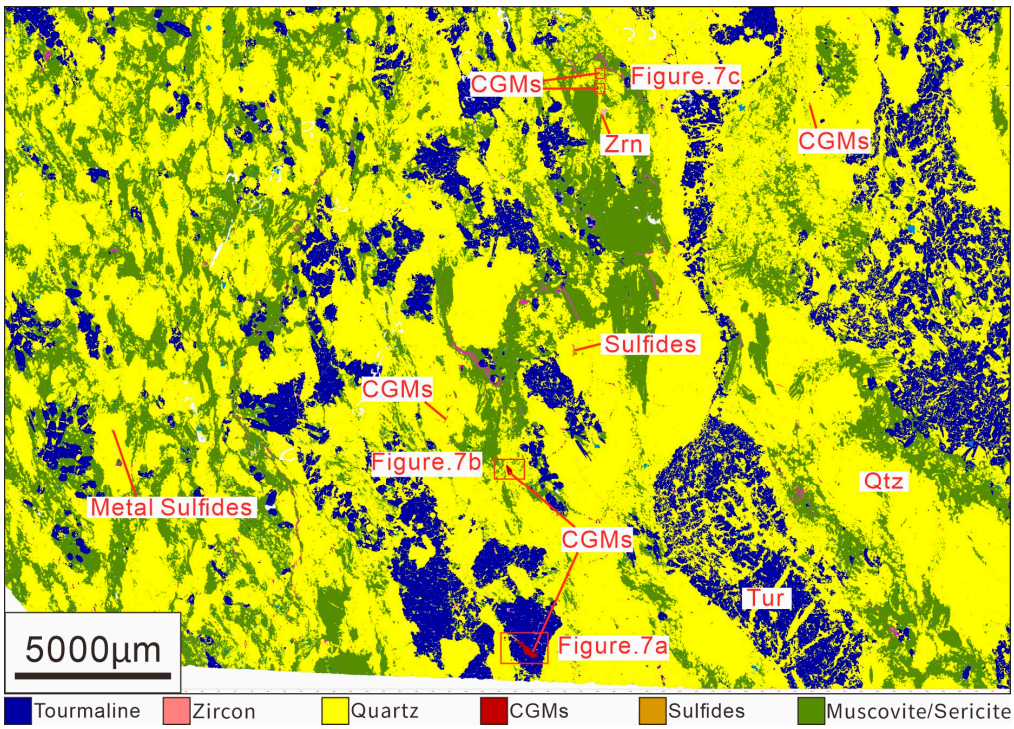


Figure 6. Mineral compositions of Nb-Ta-mineralized greisen in the Qidashan iron deposit interpreted by automated mineralogy (AMICS). The minerals in the greisen are mainly quartz, muscovite and/or tourmaline, as well as minor CGMs, sulfides, and zircon. CGMs were the main identified Nb-Ta-bearing mineral.

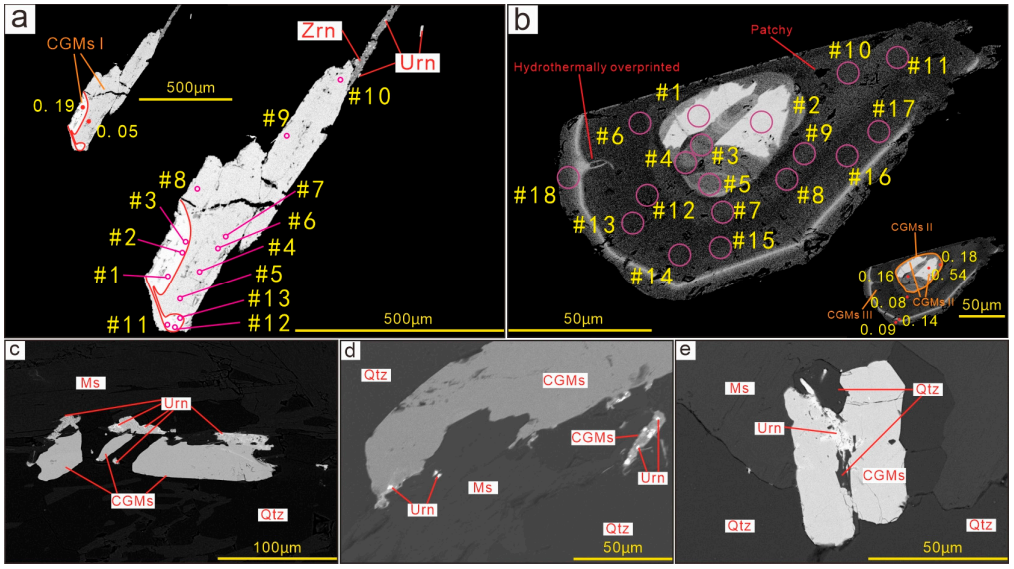


Figure 7. SEM images of CGMs in greisen-hosted Nb-Ta mineralization at Qidashan iron deposit. (**a**) CGM IIs overgrow on CGM Is with hydrothermally overprinted texture. Red points show Ta/(Nb + Ta) ratios and purple points show locations of $^{207}Pb/^{206}Pb$ analysis spots. (**b**) CGM IIIs overgrow on CGM IIs, with pseudomorphic texture of CGM Is. Red points show Ta/(Nb + Ta) ratios and purple points show locations of $^{207}Pb/^{206}Pb$ analysis spots. (**c**–**e**) Homogeneous CGM IIIs with anhedral texture and U enrichment. Abbreviations: CGMs—columbite-group minerals; Ms—muscovite; Qtz—quartz; Ser—sericite; Tur—tourmaline; Urn—uraninite; Zrn—zircon.

4.2. Major Elemental Compositions of CGMs

Representative EPMA results for CGMs from CGM Is, CGM IIs and CGM IIIs are provided in Table 1. Formation details, including the Mn#, Ta# and Ta/(Nb + Ta) ratios, can be found in Supplementary Table S1.

Table 1. EPMA results of CGM Is, CGM IIs and CGM IIIs.

CGM Type	Nb_2O_5 wt.%	Ta_2O_5	FeO	MnO	WO_3	TiO_2	Total
CGM I	68.6	7.1	16.4	4.7	1.6	1.2	98.4
	69.5	5.8	15.7	5.4	1.5	1.1	97.8
	69.2	6.6	17.4	3.9	1.6	1.2	98.7
CGM II	57.6	17.6	17.0	3.0	2.3	1.4	97.5
	60.5	14.6	17.0	3.2	2.2	1.5	97.5
	55.4	20.7	16.9	3.0	2.0	1.5	98.1
	57.3	18.8	17.0	3.0	2.0	1.7	98.0
	56.3	19.8	17.1	3.0	1.5	1.7	97.6
	53.3	22.4	16.5	3.0	2.2	1.8	97.4
	60.2	15.1	17.0	3.1	1.7	1.8	97.1
	26.1	50.9	14.6	2.6	2.5	1.8	96.6
	26.3	51.3	14.6	2.5	2.4	1.8	97.1
	25.8	52.5	14.7	2.5	2.1	1.9	97.6
	59.3	16.0	16.8	3.2	2.0	1.6	97.3
	55.4	20.4	16.9	3.1	2.1	1.6	97.9
	26.6	51.6	14.3	2.7	2.5	1.8	97.7
	53.0	24.4	16.4	3.0	2.3	1.4	99.1
	55.5	21.2	16.8	3.2	2.0	1.5	98.7
	54.1	21.8	16.4	3.5	2.1	1.5	97.8
	54.7	21.3	16.2	3.5	2.1	1.4	97.8
CGM III	63.8	10.9	16.9	3.7	2.6	1.8	97.9
	63.8	10.5	16.7	3.7	2.3	1.9	97.0
	59.5	16.1	16.6	3.3	1.7	1.7	97.2
	66.6	8.8	17.6	3.0	1.5	1.9	97.4
	68.0	7.7	17.7	2.9	1.4	1.8	97.8
	64.6	10.1	17.5	3.3	1.9	1.9	97.4
	66.6	7.5	17.9	3.0	1.9	2.2	97.0
	66.8	8.5	16.9	3.5	1.4	1.6	97.1
	69.2	5.1	17.0	3.9	1.6	1.4	96.8
	68.8	5.5	18.0	2.7	1.9	2.2	96.9
	68.8	4.3	16.3	4.0	2.0	1.9	95.5
	69.4	4.3	17.8	2.8	1.6	1.8	95.9
	68.0	4.2	19.0	1.6	1.9	2.4	94.6
	70.8	4.4	15.1	5.2	0.7	1.6	96.1
	68.9	4.4	15.2	4.9	2.3	1.6	95.6
	69.9	4.4	15.5	5.0	0.9	1.5	95.8
	68.1	5.9	16.3	4.1	0.9	2.1	95.2
	69.2	4.2	15.7	4.6	2.0	1.3	95.7
	71.5	4.1	16.4	4.1	1.6	1.3	97.7
	70.5	4.4	15.1	5.3	1.4	1.4	96.6

Table 1. *Cont.*

CGM Type	Nb_2O_5 wt.%	Ta_2O_5	FeO	MnO	WO_3	TiO_2	Total
CGM III	70.3	4.0	16.3	4.0	1.1	1.7	95.6
	68.9	4.3	16.7	4.2	2.4	1.6	96.5
	67.9	4.4	17.4	3.1	2.4	2.2	95.1
	69.9	3.5	15.6	4.8	1.8	1.7	95.6
	69.0	4.6	17.7	3.3	1.4	1.6	95.9
	67.5	6.7	16.2	4.6	0.7	1.5	95.8
	67.8	6.6	17.3	3.9	1.6	1.5	97.2
	66.4	6.7	17.3	3.6	1.6	1.5	95.5

The AMICS results suggest that all the identified Nb-Ta-bearing minerals in the greisen are classified as CGMs (Figure 6). The general formula of CGMs is AB_2O_6, where A = Fe, Mn and B = Nb, Ta, with Mn-Fe and Ta-Nb exhibiting isomorphic substitution [53,54]. CGM Is, CGM IIs and CGM IIIs in the Nb-Ta-mineralized greisens at Qidashan fall within the ideal compositional fields defined by Nb + Ta = 2.0 apfu and Nb + Ta = 1.8 apfu (Figure 8a) [24,55,56].

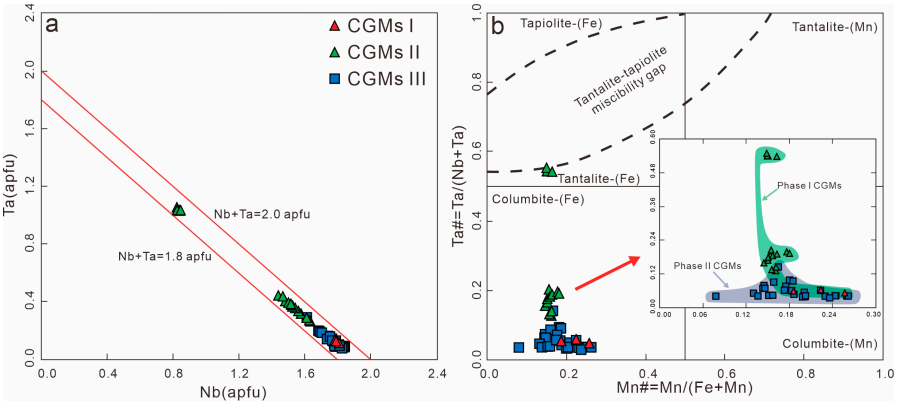


Figure 8. (**a**) Graph presents atomic proportions of Ta and Nb of the examined oxides. (**b**) Ta/(Nb + Ta) versus Mn/(Fe + Mn) diagram (apfu) showing the composition of columbite-group minerals.

CGM Is contain 68.6–69.6 wt.% Nb_2O_5, 5.8–7.1 wt.% Ta_2O_5, 15.7–17.4 wt.% FeO, and 3.9–5.4 wt.% MnO, exhibiting low Ta/(Nb + Ta) (Ta#) (0.05–0.06) and high Mn/(Fe + Mn) (Mn#) ratios (0.19–0.26), and belonging to columbite-Fe (Figure 8b). However, CGM IIs contain 25.7–60.5 wt.% Nb_2O_5, 14.6–52.5 wt.% Ta_2O_5, 14.3–17.1 wt.% FeO, and 2.5–3.5 wt.% MnO, exhibiting high Ta# values (0.13–0.55) and concentrated Mn# values (0.15–0.18), with some belonging to columbite-Fe and others to tantalite-Fe (Figure 8b). Additionally, CGM IIIs contain 59.5–71.5 wt.% Nb_2O_5, 3.5–16.2 wt.% Ta_2O_5, 15.1–19.0 wt.% FeO, and 1.60–5.3 wt.% MnO, displaying lower Ta# values (0.03–0.14) and a wider range of Mn# values (0.08–0.26), and belonging to columbite-Fe (Figure 8b). The major elemental compositions for CGM IIIs are reliable, although the total content of the elements presented in Table 1 for CGM IIIs is always less than 97 wt.%, and the rare earth elements and uranium may account for the omission, as CGM IIIs were usually altered or replaced by uraninite (Figure 7d,e) and Y, Ce, Nd, Sm, and U were detected by SEM-EDS with their total content below 1.0 wt.%. Overall, the CGMs in stage I had higher Ta# values and a narrower range of Mn# values compared to the CGMs in stage II (Figure 8b).

The EPMA mapping for CGM IIIs, which overgrow on CGM IIs, also showed that the CGMs were complexly zoned with highly variable Ta, W, Nb and restricted Al, Fe, Mn, and Ti, with U enrichment at the rim (Figure 9). CGM IIs showed pseudomorphs of CGM Is and Ta enrichment inside. CGM IIIs are characterized by faint oscillatory zoning and hydrothermal overprinting at the rim. The distribution characteristics of the elements are consistent with the phenomena observed by SEM.

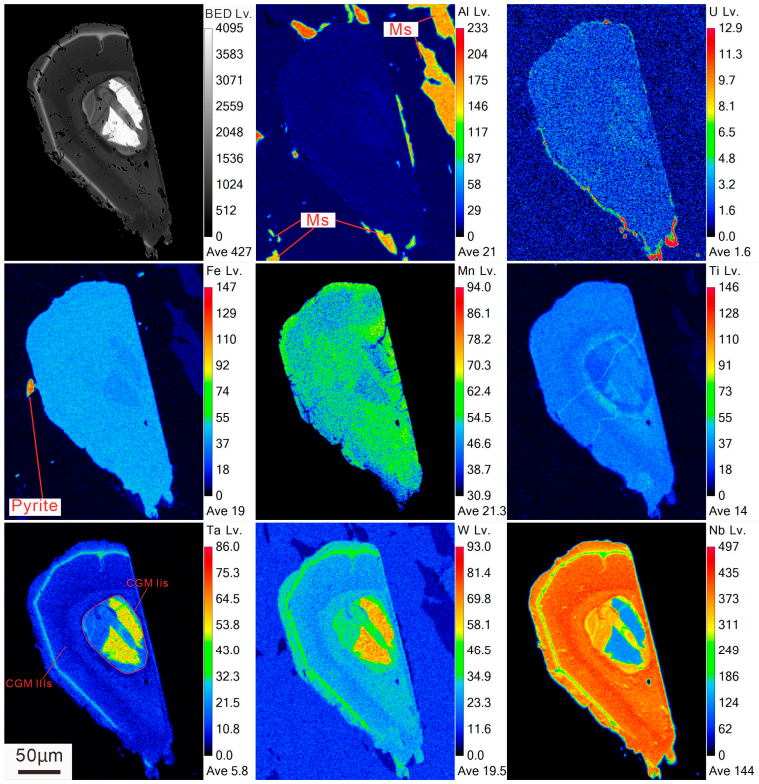


Figure 9. Distributions of Al-U-Fe-Mn-Ti-Ta-W-Nb contents in CGMs in different generations with complex texture via an EPMA. The interior of CGM IIs showed the significant enrichment of Ta, and CGM IIIs showed weak oscillating zoning.

4.3. Crystallization Age of CGMs

Representative LA-ICP-MS U-Pb dating results for CGMs from both stage I and stage II are provided in Table 2.

Table 2. LA-ICP-MS U-Pb dating results for CGM Is, CGM IIs and CGM IIIs, corrected by Coltan139.

Stage	No.	Pb^{207}/U^{235}	Pb^{207}/U^{235}_2SE (int)	Pb^{206}/U^{238}	Pb^{206}/U^{238}_2SE (int)	Pb^{207}/Pb^{206}	Pb^{207}/Pb^{206}_2SE (int)	Pb^{206}/U^{238} Age	Pb^{206}/U^{238} Age_2SE (int)	Pb^{207}/U^{235} Age	Pb^{207}/U^{235} Age_2SE (int)
I	1	11.1	0.7	0.503	0.025	0.1576	0.0020	2625	108	2525	56
	2	11.3	0.4	0.498	0.016	0.1629	0.0003	2604	70	2544	32
	3	11.9	1.1	0.511	0.027	0.1626	0.0009	2628	118	2531	60
	4	11.66	0.23	0.518	0.009	0.1639	0.0007	2689	38	2577	19
	5	11.34	0.26	0.500	0.011	0.1630	0.0004	2612	47	2550	21
	6	10.83	0.13	0.503	0.006	0.1565	0.0004	2624	25	2507	11
	7	11.03	0.21	0.504	0.009	0.1596	0.0004	2630	41	2524	18
	8	15.7	1.3	0.519	0.028	0.213	0.007	2676	120	2814	76
	9	11.8	0.4	0.506	0.014	0.1608	0.0014	2641	58	2586	31
	10	11.38	0.18	0.510	0.009	0.16290	0.00029	2654	37	2553	14
	11	11.2	0.3	0.499	0.009	0.1527	0.0014	2609	37	2538	29
	12	11.11	0.14	0.501	0.008	0.16088	0.00016	2613	36	2532	12
	13	11.48	0.17	0.521	0.008	0.1591	0.0005	2701	33	2561	14
	1	11.5	0.3	0.515	0.015	0.1613	0.0003	2673	62	2562	27
	2	10.3	0.8	0.50	0.04	0.1525	0.0006	2618	170	2460	73
	3	11.52	0.15	0.507	0.007	0.16629	0.00027	2643	28	2565	13
	4	11.36	0.17	0.515	0.007	0.1603	0.0004	2675	31	2550	14
	5	11.24	0.18	0.511	0.008	0.1630	0.0004	2657	34	2540	15

Table 2. *Cont.*

Stage	No.	Pb^{207}/U^{235}	Pb^{207}/U^{235}_2SE (int)	Pb^{206}/U^{238}	Pb^{206}/U^{238}_2SE (int)	Pb^{207}/Pb^{206}	Pb^{207}/Pb^{206}_2SE (int)	Pb^{206}/U^{238} Age	Pb^{206}/U^{238} Age_2SE (int)	Pb^{207}/U^{235} Age	Pb^{207}/U^{235} Age_2SE (int)
II	6	10.11	0.15	0.460	0.006	0.15967	0.00020	2438	28	2442	13
	7	10.41	0.16	0.465	0.008	0.16311	0.00019	2457	34	2469	14
	8	10.5	0.5	0.486	0.023	0.1577	0.0015	2530	99	2455	45
	9	11.0	0.3	0.497	0.014	0.1600	0.0008	2599	63	2508	29
	10	10.35	0.15	0.464	0.006	0.16318	0.00029	2454	29	2467	13
	11	10.70	0.16	0.487	0.007	0.1599	0.0004	2556	31	2495	14
	12	10.28	0.15	0.471	0.007	0.15875	0.00028	2484	30	2458	14
	13	10.91	0.15	0.487	0.006	0.1626	0.0003	2557	26	2516	12
	14	10.55	0.12	0.473	0.005	0.16225	0.00024	2494	23	2482	11
	15	10.52	0.14	0.472	0.006	0.16146	0.00027	2490	27	2479	13
	16	10.5	0.3	0.477	0.013	0.1589	0.0004	2504	59	2467	28
	17	10.53	0.11	0.485	0.005	0.15818	0.00021	2547	20	2481	10
	18	10.26	0.14	0.462	0.006	0.16113	0.00028	2449	27	2456	13

The apparent $^{207}Pb/^{206}Pb$ ages of CGM I (n = 7) and CGM II (n = 11) grains in stage I ranged from 2604 to 2701 Ma. These analytical spots were concordant (Figure 10a) and yielded a weighted mean $^{207}Pb/^{206}Pb$ age of 2648 ± 15 Ma (MSWD = 2.1, n = 18; Figure 10b). However, the apparent $^{207}Pb/^{206}Pb$ ages of CGM III grains (n = 13) in stage II ranged from 2438 to 2599 Ma, which were evidently different from the apparent $^{207}Pb/^{206}Pb$ ages of CGM I and CGM II grains. These analytical spots were also concordant (Figure 10c) and yielded a weighted mean $^{207}Pb/^{206}Pb$ age of 2500 ± 28 Ma (MSWD = 9.9, n = 13; Figure 10d).

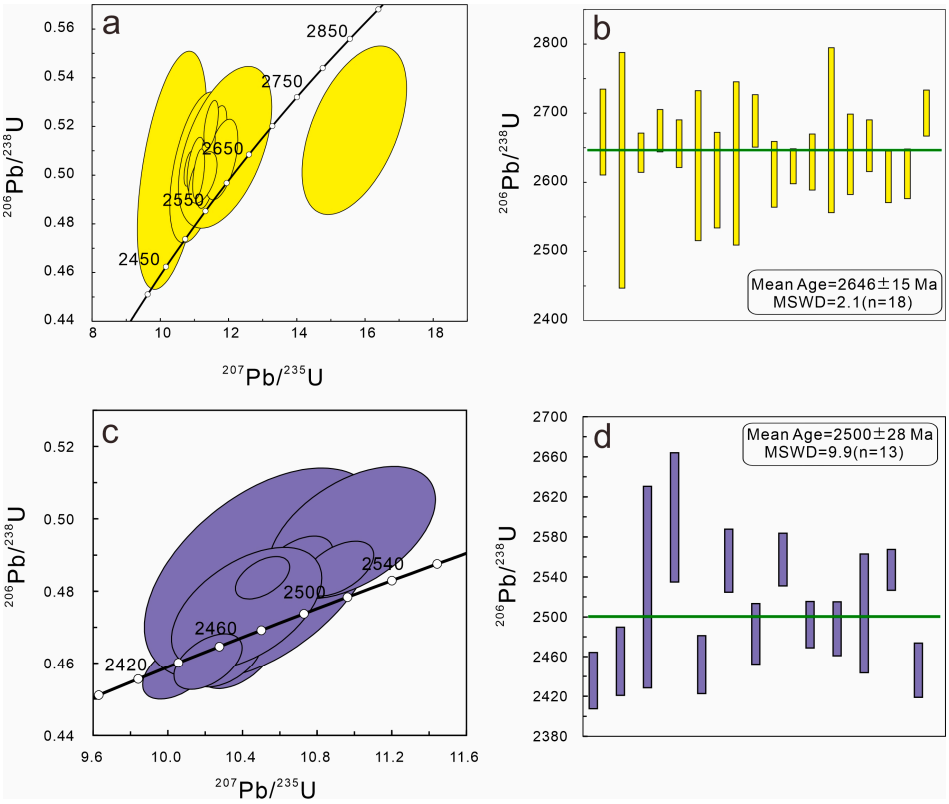


Figure 10. Concordia diagram for U-Pb ages (**a**) and weighted mean $^{207}Pb/^{206}Pb$ age (**b**) for CGMs in stage I. Concordia diagram for U-Pb ages (**c**) and weighted mean $^{207}Pb/^{206}Pb$ age (**d**) for CGMs in stage II.

5. Discussion

5.1. Characteristics and Mechanisms of Two-Stage Nb-Ta Mineralization

In the Qidashan iron deposit, greisen-hosted Nb-Ta mineralization is characterized by the formation of large amounts of CGMs (Figures 6 and 8a). The complex textures

and three generations of CGMs may be indicative of multistage Nb-Ta mineralization. CGM Is and CGM IIs are commonly associated with tourmaline or enclosed by CGM IIIs (Figures 5a–c and 7a,b). They are generally over 100 μm in grain size, and they are characterized by a wide range and generally high Ta# values (0.06–0.55), along with restricted Mn# values (0.14–0.19) (Figure 8b). This may indicate that CGM Is and CGM IIs are the products of the same mineralization stage. However, CGM IIIs are typically intergrown with muscovite and quartz, and locally enclose CGM IIs and/or CGM Is (Figures 5c–i and 7b–e). They are usually less than 50 μm in grain size, and they are characterized by low Ta# values and variable Mn# values (Figure 8b). The formation of CGM IIIs may therefore be related to the late mineralization stage.

The complex zoning textures of CGMs contains abundant origin information, which can be typically distinguished between magmatic and hydrothermal processes [2,4–8]. CGM Is show a large size (>100 μm) and are euhedral and homogeneous (Figure 7a), interpreted to be of magmatic origin [6]. CGM IIs overgrow on CGM Is at the rim or locally pseudomorphously replace CGM Is, showing an irregular boundary (Figure 7a,b), which is regarded as hydrothermally overprinting [4,7,24,57–61]. These homogeneous and overprinting textures reveal that the formation of CGM Is and CGM IIs involve a transition from magmatic to magmatic–hydrothermal conditions during mineralization stage I. Chemically, CGM IIs show a distinct compositional gap from CGM Is, marked by a significant increase in Ta# (Figure 8b). However, previous experimental studies have indicated that the fluid/melt partition coefficient of Ta is very low [62,63]. Under conditions of 300–550 °C and 50–100 MPa, the solubility of Ta in hydrothermal fluids is lower than that of Nb [64]. Consequently, it is difficult to explain the formation of high-Ta# CGMs through a conventional hydrothermal process. However, a supercritical phase—referred to as a hydrosilicate fluid—has been identified through studies of melt–melt–fluid immiscibility in melt inclusions [65,66]. It is characterized by a SiO_2/H_2O molar ratio near unity, a low density, and a low viscosity, distinguishing it from conventional hydrothermal fluids [59,67–69], and it can dissolve high concentrations of Ta from approximately 600 °C down to the lower temperatures [70]. Ta-enriched "hydrosilicate fluid" can replace CGM Is through partial dissolution, resulting in hydrothermally overprinting textures for CGM IIs [71–74]. CGM IIIs are also attributed to hydrothermal activity, based on their anhedral texture and mutual replacement with the coarse-grained muscovite, indicative of a hydrothermal fluid origin (Figures 5d–i and 7c–e). However, CGM IIIs can also overgrow on CGM IIs and/or CGM Is, with faint oscillatory zoning [57,58] and overprinting of their rims (Figure 7b). The genesis of oscillatory zoning with pervasive patchy and porous texture is interpreted as the result of slow elemental diffusion [75] (Figure 7b), indicating a hydrothermal origin [59–61] rather than rapid-disequilibrium crystallization from magma [76].

5.2. Geological Background of the Two-Stage Nb-Ta Mineralization

CGMs are widely used for dating pegmatites, granites, and other felsic intrusions due to their high U and low common Pb contents [77–79]. Conventional CGM U-Pb dating typically employs spot sizes of 45–90 μm, which limits the ability to resolve age domains in compositionally zoned crystals. Recently, methodological advances have enabled U-Pb dating with spot sizes as small as 10 μm. The accuracy of this refined approach has been validated on homogeneous CGMs from the Dakalasu and Jingerquan deposits in the Altai and East Tianshan orogenic belts, Xinjiang, China [16]. To ensure analytical reliability, we employed a 15 μm spot size and obtained two distinct weighted mean $^{206}Pb/^{238}U$ ages: 2648 ± 15 Ma and 2500 ± 28 Ma. The younger age is consistent with the CGM U-Pb age reported by Yao et al. using a 45 μm spot, further supporting the reliability of our results [29]. We therefore consider this improved U-Pb dating method to be applicable to

the greisen-hosted Nb-Ta mineralization at Qidashan. The weighted mean U-Pb ages of CGMs from stage I and stage II were 2648 ± 15 Ma and 2500 ± 28 Ma, respectively. They represent the two-stage Nb-Ta mineralization at ~2.7 Ga and 2.5 Ga.

The CGMs of stage I formed at ~2.7 Ga, which belongs to the "quiet period" of 2.55–2.95 Ga in the Anshan–Benxi area [43]. The "quiet period" of 2.55–2.95 Ga was proposed probably due to the absence of exposed contemporaneous granitic plutons or their obliteration by later processes. However, magmatic zircons of 2.72–2.65 Ga have been reported in the Neoarchean Anshan metamorphic rocks of greenschist-facies in the Anshan area [51], suggesting a ~2.7 Ga submarine volcanic–thermal event potentially linked to the formation of BIFs in these sedimentary–metamorphic iron deposits. Previous reconstructions of protoliths have indicated that the plagioclase amphibolites of the Yingtaoyuan Formation in the Qidashan iron deposit originated from mafic igneous sources, while the schists were derived from pelitic or siltstone origins [80]. These meta-pelites and siltstones in the seafloor may provide potential source materials for LCT-type pegmatites (S-type granites), which can yield significant rare metal elements [67,81]. Consequently, we proposed that high-temperature basaltic magmatism (1000–1200 °C) during this period can generate local thermal anomalies, leading to the partial melting of pelitic/siltstone sequences that account for the early Nb-Ta enrichment in magmatic and hydrothermal processes. The formation of CGMs in stage II is associated with the metasomatic alteration of the early Nb-Ta-enriched pluton formed in ~2.7 Ga as a result of the emplacement of the Qidashan granite at 2.5 Ga. Widespread Archean mineralization of rare metals along the eastern North China Craton margin has been reported, including the 2.5 Ga LCT-type pegmatite in Yanlingguan (Shandong Province) [82], 2.51–2.49 Ga Nb-Ta granitic pegmatite in Lijiapuzi (Liaoning Province) [83], and ~2.5 Ga Nb-Ta mineralization in albitized granites at Gongchangling (Liaoning Province) [84], suggesting that these mineralizations may correspond to a regional tectono-thermal event at ~2.5 Ga [49,85]. The 2.5 Ga Qidashan granite, likely produced by melting of older continental crust under extensive conditions [46,49], shows a temporal coincidence with the 2.5 Ga Nb-Ta mineralization. Previous studies have documented hydrothermal mineral assemblages in chlorites and geochemical inheritance between greisen and the granite, suggesting that the chlorites, greisen, and CGMs of stage II may result from autometasomatism by "hydrosilicate fluids" evolved from the Qidashan granitic magma [29]. The formation of these Nb-Ta-mineralized greisen was therefore regarded as the superimposition and reworking of the early Nb-Ta-enriched pluton at ~2.7 Ga by "hydrosilicate fluid", which is associated with the Qidashan granite pluton, providing the ultimate Nb-Ta source.

5.3. Mineralization Process of Greisen-Hosted Nb–Ta in the Qidashan Iron Deposit

Figure 11 illustrates the ore-forming process of greisen-hosted Nb-Ta mineralization in the Qidashan iron deposit, which consists of two primary mineralization stages: stage I and stage II. Following the formation of the ancient continental nucleus, mineralization stage I took place in the Anshan–Benxi area, accompanied by the commencement of submarine volcanic activity at ~2.7 Ga. The submarine eruption of mafic magmas not only provided ore-forming iron elements for the formation of BIFs, but also created localized geothermal anomalies. These geothermal anomalies facilitated the partial melting of psammitic–pelitic seafloor sediments, resulting in the formation of an early Nb-Ta-enriched silicate melt (Figure 11a) and subsequent precipitation of CGM Is and CGM IIs, which are generally coeval with tourmaline. The occurrence of tourmaline usually indicates the enrichment of volatile components, especially boron. Volatile components are commonly regarded as fluxes in the silicate melt, lowering crystallization temperature of the melt [24,86–88] and resulting in the partial melting of fusible minerals, such as quartz and mica, under

local thermal anomalies. Given the high incompatibilities of Nb and Ta, these elements preferentially concentrated in the silicate melt during partial melting, ultimately leading to an enriched melt for both Nb and Ta (Figure 11b). Accompanied by the evolution of these silicate melts, CGM Is began to crystallize during the late magmatic stage. They are characterized by coarse grains (>100 μm) with a euhedral and homogeneous texture (Figure 11b). During the subsequent transition from magma to magmatic hydrothermal fluid, Ta-enriched "hydrosilicate fluids" exsolved from the silicate melt. These fluids replaced and altered CGM Is, forming high-Ta# CGM IIs with a hydrothermally overprinting texture (Figure 11b). CGM Is and CGM IIs were ultimately overgrown by tourmaline (Figure 11b), suggesting that tourmaline crystallization persisted into the hydrothermal stage. Tourmaline can play an important role in Mn/Fe fractionation [24], resulting in the relatively narrow range of Mn# observed in CGM Is and CGM IIs (Figure 8b).

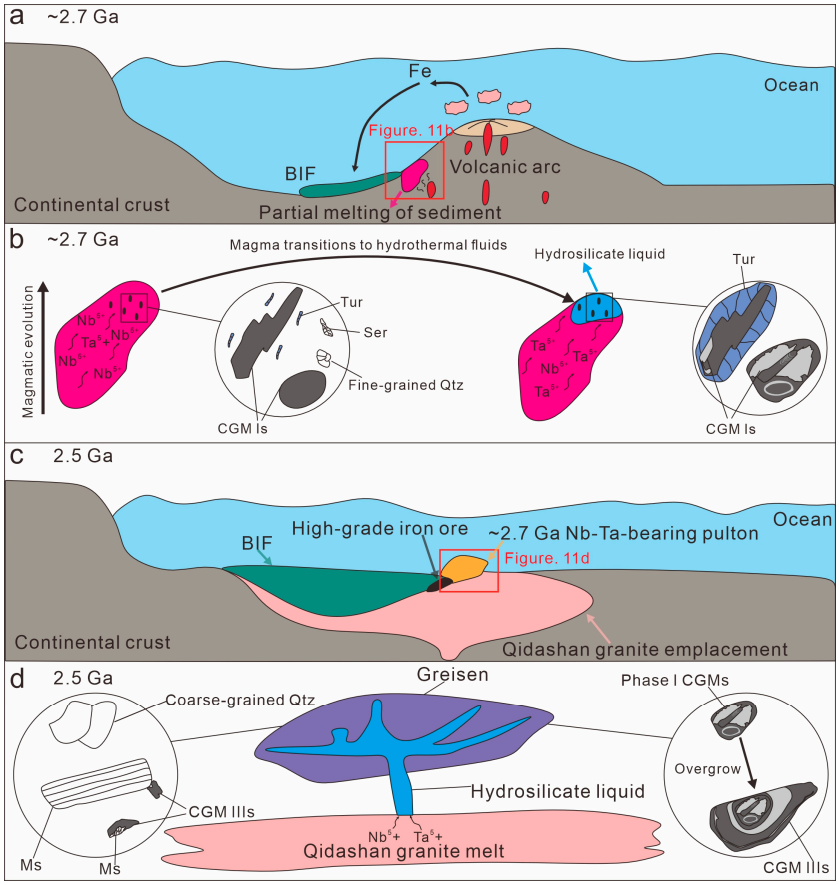


Figure 11. Schematic diagram showing the genesis of greisen-hosted Nb-Ta mineralization and iron ore formation. (**a**) At ~2.7 Ga, submarine volcanism supplied the iron for BIFs. The eruption of high-temperature mafic magmas simultaneously induced local geothermal anomalies, which gave rise to partial melting of the sediments. (**b**) With magmatic evolution and concurrent Nb-Ta enrichment, homogeneous CGM Is crystallized along with tourmaline in the late magmatic stage. During the magmatic–hydrothermal transition, "hydrosilicate fluids" metasomatized CGM Is, forming hydrothermally overprinted CGM IIs, which were subsequently enclosed by tourmaline. (**c**) The intrusion of the Qidashan granite resulted in both the upgrading of the BIF into high-grade iron ore and the metasomatism of the earlier Nb–Ta-rich rocks. (**d**) Hydrosilicate fluids derived from the Qidashan granite metasomatized earlier rock units to form greisen. During this process, sericite and fine-grained quartz recrystallized into muscovite and coarse quartz. The homogeneous, anhedral CGM IIIs either showed mutual replacement with sericite or were intergrown with muscovite, while the zoned CGM IIIs overgrew on CGM IIs and/or CGM Is. Abbreviations: CGMs—columbite-group minerals; Ms—muscovite; Qtz—quartz; Ser—sericite; Tur—tourmaline.

Mineralization stage II occurred at 2.5 Ga together with the emplacement of the Qidashan granite, which originated from the early crustal materials and enriched Nb-Ta in the residual melt during the magmatic evolution [46]. The residual melt formed magmatic CGMs in the Qidashan granite with U-Pb ages of 2505–2527 Ma [29,46], and released Nb-Ta-enriched "hydrosilicate fluids" [29], which metasomatized the ~2.7 Ga Nb-Ta-enriched pluton and resulted in the formation of greisen (Figure 11c). The "hydrosilicate fluids" also locally remobilized iron from BIFs, leading to the generation of high-grade iron ore (Figure 11c) [29]. The consistent association of CGM IIIs with coarse-grained muscovite and quartz indicates that they crystallized together through fluid metasomatism. This mineral assemblage is believed to have formed from the recrystallization of fine-grained sericite and quartz. Furthermore, the typically anhedral, hydrothermally overprinted and patchy textures suggest that hydrothermal fluid activity was involved in their formation. Consequently, mineralization stage II was exclusively dominated by "hydrosilicate fluid" metasomatism. These fluids metasomatized the ~2.7 Ga Nb-Ta-rich pluton, resulting in the recrystallization of muscovite and coarse-grained quartz, and simultaneous precipitation of CGM IIIs (Figure 11d).

5.4. Implications for Nb–Ta Mineralization and Regional Exploration

The relative contributions of magmatic and magmatic hydrothermal processes to enrichment and Nb-Ta mineralization have been a subject of considerable debate. Many researchers contend that Nb-Ta mineralization primarily results from magmatic differentiation, during which these elements become increasingly concentrated in the melt throughout magmatic evolution until reaching saturation [15]. This process leads to the crystallization of either homogeneous or zoned CGMs [7,15,26]. However, the role of hydrosilicate fluids in Nb-Ta mineralization is garnering increasing attention [8,15–18,38]. The investigation of greisen-hosted Nb-Ta mineralization at Qidashan demonstrates that both stage I and stage II indicate the presence of "hydrosilicate fluids". Moreover, the formation of greisen and greisen-hosted Nb-Ta mineralization was dominated by these hydrosilicate fluids, which are capable of transporting and precipitating Nb and Ta as CGMs, as well as fractionating Nb from Ta. This fractionation potential suggests the ability to produce higher-value tantalite. These findings indicate that hydrosilicate fluids likely play an essential role in Nb-Ta mineralization at Qidashan, and other altered rock-hosted Nb-Ta mineralization elsewhere.

The greisen-hosted Nb-Ta mineralization in the Qidashan iron deposit occurred during two distinct periods, at ~2.7 Ga and ~2.5 Ga, which are linked to the development of BIFs and the formation of high-grade iron ore, respectively. This association suggests that sedimentary–metamorphic iron deposits in the Anshan–Benxi area, as well as Algoma-type iron deposits worldwide with similar geological settings, may possess potential for altered rock-hosted Nb-Ta mineralization. Similar Nb-Ta mineralization related to high-grade iron ores has been documented in the adjacent Gongchangling iron deposit [84]. In particular, the dominated Nb-Ta mineralization in stage II at ~2.5 Ga shows a close spatial and temporal association with the Qidashan granite pluton, indicating that both the pluton and the surrounding greisen possess significant potential for Nb-Ta mineralization. Meanwhile, several ~2.5 Ga granite–pegmatite Nb-Ta rare metal deposits along the northern margin of the North China Craton, such as Yanlingguan and Lijiapuzi, have been reported [82,83]. We therefore propose that the North China Craton likely holds significant potential for Precambrian Nb-Ta mineralization, similar to other ancient cratons worldwide [89], and deserves greater attention in future mineral exploration for these critical metals.

6. Conclusions

(1) Niobium and tantalum are exclusively hosted within columbite-group minerals (CGMs), and three generations of CGMs are distinguished: CGM Is, CGM IIs and CGM IIIs. The textural and chemical features of CGMs indicate a magmatic origin of CGM Is and a hydrothermal fluid replacement origin of CGM IIs and CGM IIIs.

(2) Two distinct mineralization stages of CGMs have been identified: CGM Is and CGM IIs of stage I yield crystallization ages of 2646 ± 15 Ma, and their origin is related to submarine volcanism associated with BIF formation; CGM IIIs of stage II record younger formation at 2500 ± 28 Ma, suggesting that stage II is linked to the emplacement of the Qidashan granite.

(3) Mineralization stage I experienced a transition from magma to "hydrosilicate fluid", resulting in the precipitation of CGMs I and CGMs II and the formation of the ~2.7 Ga Nb-Ta-enriched pluton. Mineralization stage II was solely controlled by "hydrosilicate fluid" related to the Qidashan granite, resulting in the formation of CGM IIIs and greisen, as well as the high-grade iron ore.

(4) Significant Precambrian Nb-Ta mineralization potential was proposed in Algoma-type iron deposits within the Anshan–Benxi area along the northern margin of the North China Craton and comparable Algoma-type iron deposits globally.

Supplementary Materials: The following supporting information can be downloaded at: https://www.mdpi.com/article/10.3390/min16030312/s1, Table S1: Chemical compositions of CGMs in the greisen from the Qidashan iron deposit, analyzed by EMPA.

Author Contributions: Conceptualization, Y.X. and R.G.; Data Curation, Y.X., R.G., Q.S., S.J. and J.C.; Writing—Original Draft, Y.X.; Writing—Review and Editing, R.G.; Validation, R.G., J.F. and Y.Y.; Investigation, Y.X., R.G., Y.Y., J.F., S.J. and J.C. All authors have read and agreed to the published version of the manuscript.

Funding: This research was jointly supported by the National Key Research and Development Program of China for Young Scientists (2022YFC2905400), the National Natural Science Foundation of China (41902067), the Natural Science Foundation of Liaoning Province (2023-MSBA-116) and the Fundamental Research Funds for the Central Universities (N2124002-10).

Data Availability Statement: The authors declare that all analytical data supporting the findings of this study are available within the paper and its Supplementary Information Files or cited peer-review references.

Acknowledgments: We appreciate Wuhan Sample Solution Analytical Technology Co., Ltd., for its EPMAs, and China University of Geosciences, CUGB, for its CGM U-Pb dating analyses. We are deeply indebted to Yongzeng Wang for his kind help in field investigations and sampling. We are grateful for the insightful suggestions from three anonymous reviewers, which greatly improved our manuscript.

Conflicts of Interest: The authors declare that they have no known competing financial interests or personal relationships that could have appeared to influence the work reported in this paper.

References

1. Gulley, A.L.; Nassar, N.T.; Xun, S. China, the United States, and competition for resources that enable emerging technologies. *Proc. Natl. Acad. Sci. USA* **2018**, *115*, 4111–4115. [CrossRef] [PubMed]
2. Linnen, R.L.; Van Lichtervelde, M.; Černý, P. Granitic pegmatites as sources of strategic metals. *Elements* **2012**, *8*, 275–280. [CrossRef]
3. Weng, Z.; Jowitt, S.M.; Mudd, G.M.; Haque, N. A detailed assessment of global rare earth element resources: Opportunities and challenges. *Econ. Geol.* **2015**, *110*, 1925–1952. [CrossRef]
4. Novak, M.; Cerny, P. Niobium-tantalum oxide minerals from complex granitic pegmatites in the Moldanubicum, Czech Republic; primary versus secondary compositional trends. *Can. J. Miner. Petrol.* **1998**, *36*, 659–672.

5. Tindle, A.G.; Breaks, F.W. Columbite-tantalite mineral chemistry from rare-element granitic pegmatites: Separation Lakeh area, N.W. Ontario, Canada. *Miner. Petrol.* **2000**, *70*, 165–198. [CrossRef]
6. Van Lichtervelde, M.; Salvi, S.; Beziat, D.; Linnen, R.L. Textural features and chemical evolution in tantalum oxides: Magmatic versus hydrothermal origins for Ta mineralization in the Tanco Lower Pegmatite, Manitoba, Canada. *Econ. Geol.* **2007**, *102*, 257–276. [CrossRef]
7. Wu, M.; Samson, I.M.; Zhang, D. Textural and chemical constraints on the formation of disseminated granite-hosted W-Ta-Nb mineralization at the Dajishan Deposit, Nanling Range, Southeastern China. *Econ. Geol.* **2017**, *112*, 855–887. [CrossRef]
8. Zhang, L.; Jiang, S.; Romer, R.L.; Su, H. Relative importance of magmatic and hydrothermal processes for economic Nb-Ta-W-Sn mineralization in a peraluminous granite system: The Zhaojinggou rare-metal deposit, northern China. *Geol. Soc. Am. Bull.* **2023**, *135*, 2529–2553. [CrossRef]
9. Yin, L.; Pollard, P.J.; Shouxi, H.; Taylor, R.G. Geologic and geochemical characteristics of the Yichun Ta-Nb-Li deposit, Jiangxi Province, South China. *Econ. Geol.* **1995**, *90*, 577–585. [CrossRef]
10. Linnen, R.L.; Keppler, H. Columbite solubility in granitic melts: Consequences for the enrichment and fractionation of Nb and Ta in the Earth's crust. *Contrib. Mineral. Petrol.* **1997**, *128*, 213–227. [CrossRef]
11. Linnen, R.L. The solubility of Nb-Ta-Zr-Hf-W in granitic melts with Li and Li + F; constraints for mineralization in rare metal granites and pegmatites. *Econ. Geol.* **1998**, *93*, 1013–1025. [CrossRef]
12. Ballouard, C.; Poujol, M.; Boulvais, P.; Branquet, Y.; Tartèse, R.; Vigneresse, J. Nb-Ta fractionation in peraluminous granites: A marker of the magmatic-hydrothermal transition. *Geology* **2016**, *44*, 231–234. [CrossRef]
13. Zhu, Z.; Wang, R.; Marignac, C.; Cuney, M.; Mercadier, J.; Che, X.; Charles, N.; Lespinasse, M. Petrogenesis of Nb–(Ta) aplo-pegmatites and fine-grained granites from the early Cretaceous Huangshan rare-metal granite suite, northeast Jiangxi Province, southeast China. *Lithos* **2019**, 346–347, 105150.
14. Wu, H.; Huang, H.; Zhang, Z.; Wang, T.; Guo, L.; Zhang, Y.; Wang, W. Geochronology, geochemistry, mineralogy and metallogenic implications of the Zhaojinggou Nb-Ta deposit in the northern margin of the North China Craton, China. *Ore Geol. Rev.* **2020**, *125*, 103692. [CrossRef]
15. Hetherington, C.J.; Mailloux, G.A.; Miller, B.V. A multi-mineral U-(Th)-Pb dating study of the Stetind pegmatite of the Tysfjord region, Norway, and implications for production of NYF-rare element pegmatites during orogenic collapse. *Lithos* **2021**, 398–399, 106257.
16. Yang, S.; Zhang, L.; Wang, R.; Zhu, D.; Xie, J.; Wang, Q.; Xu, W. Application of high-resolution laser multi collector ICP-MS U–Pb dating to columbite-group minerals with compositional zonation: Reassessment of matrix effects among columbite-group minerals. *J. Anal. At. Spectrom.* **2024**, *39*, 2421–2432. [CrossRef]
17. Černý, P.; Ercit, T.S. The classification of granitic pegmatites revisited. *Can. J. Miner. Petrol.* **2005**, *43*, 2005–2026. [CrossRef]
18. Wang, L.; Zhao, T.; Chen, W. Advances in study of Nb-Ta ore deposits in Panxi area and tentative discussion on genesis of these ore deposits. *Miner. Depos.* **2012**, *31*, 16.
19. Li, J.; Li, P.; Wang, D.; Li, X. A review of niobium and tantalum metallogenic regularity in China. *Chin. Sci. Bull.* **2019**, *64*, 1545–1566. [CrossRef]
20. Li, L.; Li, H.; Fu, J.; Ma, Y.; Yao, Y.; Luan, J. A new type of Nb-Ta mineralization discovered in the Neoarchean Anshan-type iron deposit of the northern North China Craton. *Geol. China* **2022**, *49*, 1353–1354.
21. Wen, C.; Shao, Y.; Huang, G.; Luo, X.; Li, M. Geochemical features and mineralization of Jianfengling rare metal granitein Hunan Province. *Miner. Depos.* **2017**, *36*, 879–892.
22. Breiter, K.; Hložková, M.; Korbelová, Z.; Galiová, M.V. Diversity of lithium mica compositions in mineralized granite–greisen system: Cínovec Li-Sn-W deposit, Erzgebirge. *Ore Geol. Rev.* **2019**, *106*, 12–27. [CrossRef]
23. Hreus, S.; Výravský, J.; Cempírek, J.; Breiter, K.; Vašinová Galiová, M.; Krátký, O.; Šešulka, V.; Škoda, R. Scandium distribution in the world-class Li-Sn-W Cínovec greisen-type deposit: Result of a complex magmatic to hydrothermal evolution, implications for scandium valorization. *Ore Geol. Rev.* **2021**, *139*, 104433. [CrossRef]
24. Ryznar, J.; Pršek, J.; Włodek, A.; Uher, P. Mineralogy and chemistry of columbite-tantalite from Bugarura-Kuluti area, Karagwe-Ankole Belt, Rwanda: Indicators of pegmatite and granite evolution. *Ore Geol. Rev.* **2023**, *159*, 105574. [CrossRef]
25. Gong, L.; Guo, C.; Yu, M.; Zheng, Y.; Zhang, B.; Chen, Z.; Ma, X.; Xv, Y. Difference study of greisen formation between open and closed magmatic systems: Example from four representative W- and Li-bearing deposits in the Nanling metallogenic belt. *Acta Petrol. Sin.* **2024**, *40*, 2905–2924. [CrossRef]
26. Shcherba, G.N. Greisens. *Int. Geol. Rev.* **1970**, *12*, 114–150. [CrossRef]
27. Štemprok, M. Greisenization (a review). *Geol. Rundsch.* **1987**, *76*, 169–175.
28. Yuan, Z.; Bai, G.; Yang, Y. A disscussion on pertrogenesis of rare metal granites. *Miner. Depos.* **1987**, *6*, 90–98.
29. Yao, Y.; Wei, C.; Liu, J.; Fu, J.; Xu, S. Ore-forming mechanism of high-grade iron ore in Qidashan iron deposit, Liaoning Province: Insights from the columbite-group minerals in granite and altered rocks. *J. Asian Earth Sci.* **2025**, *294*, 106791. [CrossRef]
30. Zhao, G.; Wilde, S.A.; Cawood, P.A.; Sun, M. Archean blocks and their boundaries in the North China Craton: Lithological, geochemical, structural and P–T path constraints and tectonic evolution. *Precambrian Res.* **2001**, *107*, 45–73. [CrossRef]

31. Zhao, G.; Sun, M.; Wilde, S. Major tectonic units of the North China Craton and their Paleoproterozoic assembly. *Sci. China Ser. D* **2003**, *46*, 23–38. [CrossRef]
32. Zhao, G.; Sun, M.; Wilde, S.A.; Sanzhong, L. Late Archean to Paleoproterozoic evolution of the North China Craton: Key issues revisited. *Precambrian Res.* **2005**, *136*, 177–202. [CrossRef]
33. Zhai, M.; Windley, B.F. The Archaean and early Proterozoic banded iron formations of North China: Their characteristics, geotectonic relations, chemistry and implications for crustal growth. *Precambrian Res.* **1990**, *48*, 267–286. [CrossRef]
34. Guo, R.; Li, Z.; Liu, S.; Wang, M.; Bao, H.; Wang, W.; Huang, X.; Dou, Y. Late Neoarchean geodynamic regime of the northeastern North China Craton: Constraints from metamorphosed volcanic rocks of the Anshan-Benxi greenstone belt. *Precambrian Res.* **2022**, *371*, 106583. [CrossRef]
35. Wei, C.; Yao, Y.; Fu, J.; Guo, R.; Liu, J.; Jia, S.; Xiao, Y. Diverse provenances and tectonic setting of late Neoarchean metasedimentary rocks from the Anshan-Benxi greenstone belt, North China Craton: Constraints from whole-rock geochemistry and zircon U–Pb–Lu–Hf isotopes. *J. Asian Earth Sci.* **2025**, *279*, 106443. [CrossRef]
36. Wang, C.; Peng, Z.; Tong, X.; Huang, H.; Zheng, M.; Zhang, L.; Zhai, M. Late Neoarchean supracrustal rocks from the Anshan-Benxi terrane, North China Craton: New geodynamic implications from the geochemical record. *Am. J. Sci.* **2017**, *317*, 1095–1148. [CrossRef]
37. Tong, X.; Wang, C.; Peng, Z.; Huang, H.; Zhang, L.; Zhai, M. Geochemistry of meta-sedimentary rocks associated with the Neoarchean Dagushan BIF in the Anshan-Benxi area, North China Craton: Implications for their provenance and tectonic setting. *Precambrian Res.* **2019**, *325*, 172–191. [CrossRef]
38. Zhang, J.; Shao, J.; Bao, Z.; Wang, H.; Zhou, Y. Geological characterisitics and prospecting indicators for Dataigou iron deposit in Benxi, Liaoning province. *Geol. Resour.* **2014**, *23*, 343–351.
39. Tang, H.; Chen, Y.; Wu, G.; Lai, Y. Paleoproterozoic positive δ13Ccarb excursion in the northeastern Sino-Korean craton: Evidence of the Lomagundi event. *Gondwana Res.* **2011**, *19*, 471–481. [CrossRef]
40. Tang, H.; Chen, Y.; Santosh, M.; Zhong, H.; Wu, G.; Lai, Y. C–O isotope geochemistry of the Dashiqiao magnesite belt, North China Craton: Implications for the great oxidation event and ore genesis. *Geol. J.* **2013**, *48*, 467–483. [CrossRef]
41. Wu, F.; Zhang, Y.; Yang, J.; Xie, L.; Yang, Y. Zircon U–Pb and Hf isotopic constraints on the early Archean crustal evolution in Anshan of the North China Craton. *Precambrian Res.* **2008**, *167*, 339–362. [CrossRef]
42. Wang, Y.; Li, X.; Jin, W.; Zeng, L.; Zhang, J. Generation and maturation of Mesoarchean continental crust in the Anshan complex, North China Craton. *Precambrian Res.* **2020**, *341*, 105651. [CrossRef]
43. Wan, Y.; Dong, C.; Xie, H.; Liu, S.; Ma, M.; Li, P.; Li, Y.; Wang, Y.; Wang, Q.; Liu, D. Formation and evolution of Archean continental crust in the Anshan-Benxi area, North China Craton: A review. *Earth Sci.* **2024**, *49*, 3855.
44. Song, B.; Nutman, A.P.; Liu, D.; Wu, J. 3800 to 2500 Ma crustal evolution in the Anshan area of Liaoning Province, northeastern China. *Precambrian Res.* **1996**, *78*, 79–94. [CrossRef]
45. Dong, C.; Wan, Y.; Xie, H.; Nutman, A.P.; Xie, S.; Liu, S.; Ma, M.; Liu, D. The Mesoarchean Tiejiashan-Gongchangling potassic granite in the Anshan-Benxi area, North China Craton: Origin by recycling of Paleo- to Eoarchean crust from U-Pb-Nd-Hf-O isotopic studies. *Lithos* **2017**, *290–291*, 116–135. [CrossRef]
46. Dai, Y.; Li, L.; Zhang, Y. Archean Nb-Ta-bearing granites recognized in the Anshan–Benxi area, North China Craton: Petrogenesis and rare metal potential. *Precambrian Res.* **2025**, *431*, 107964. [CrossRef]
47. Wan, Y.; Ma, M.; Dong, C.; Xie, H.; Xie, S.; Ren, P.; Liu, D. Widespread late Neoarchean reworking of Meso- to Paleoarchean continental crust in the Anshan-Benxi area, North China Craton, as documented by U-Pb-Nd-Hf-O isotopes. *Am. J. Sci.* **2015**, *315*, 620–670. [CrossRef]
48. Zhao, G.; Cawood, P.A.; Li, S.; Wilde, S.A.; Sun, M.; Zhang, J.; He, Y.; Yin, C. Amalgamation of the North China Craton: Key issues and discussion. *Precambrian Res.* **2012**, *222–223*, 55–76. [CrossRef]
49. Wan, Y.; Dong, C.; Liu, D.; Kröner, A.; Yang, C.; Wang, W.; Du, L.; Xie, H.; Ma, M. Zircon ages and geochemistry of late Neoarchean syenogranites in the North China Craton: A review. *Precambrian Res.* **2012**, *222–223*, 265–289. [CrossRef]
50. Liu, Z.; Fu, H.; Liu, L. The distribution and characteristics of the very large iron ore deposits of Anshan-Benxi. *Geol. Chem. Miner.* **2015**, *37*, 65–71.
51. Li, L.; Li, H.; Liu, M.; Yang, X.; Meng, J. Timing of deposition and tectonothermal events of banded iron formations in the Anshan–Benxi area, Liaoning Province, China: Evidence from SHRIMP U-Pb zircon geochronology of the wall rocks. *J. Asian Earth Sci.* **2016**, *129*, 276–293. [CrossRef]
52. Paton, C.; Hellstrom, J.; Paul, B.; Woodhead, J.; Hergt, J. Iolite: Freeware for the visualisation and processing of mass spectrometric data. *J. Anal. At. Spectrom.* **2011**, *26*, 2508–2518. [CrossRef]
53. Černý, P.; Ercit, T.S. *Mineralogy of Niobium and Tantalum: Crystal Chemical Relationships, Paragenetic Aspects and Their Economic Implications*; Möller, P., Černý, P., Saupé, F., Eds.; Springer: Berlin/Heidelberg, Germany, 1989; pp. 27–79.
54. Cerny, P.; Roberts, W.L.; Ercit, T.S.; Chapman, R. Wodginite and associated oxide minerals from the Peerless pegmatite, Pennington County, South Dakota. *Am. Miner.* **1985**, *70*, 1044–1049.

55. Fuchsloch, W.C.; Nex, P.A.M.; Kinnaird, J.A. The geochemical evolution of Nb–Ta–Sn oxides from pegmatites of the Cape Cross–Uis pegmatite belt, Namibia. *Miner. Mag.* **2019**, *83*, 161–179. [CrossRef]
56. Neiva, A.M.R. Geochemistry of cassiterite and its inclusions and exsolution products from tin and tungsten deposits in Portugal. *Can. J. Miner. Petrol.* **1996**, *34*, 745–768.
57. Cao, C.; Shen, P.; Bai, Y.; Luo, Y.; Feng, H.; Li, C.; Pan, H. Chemical evolution of micas and Nb-Ta oxides from the Koktokay pegmatites, Altay, NW China: Insights into rare-metal mineralization and genetic relationships. *Ore Geol. Rev.* **2022**, *146*, 104933. [CrossRef]
58. Duan, Z.; Jiang, S.; Su, H.; Zhu, X.; Zou, T. Nb-Ta oxides as recorders of hydrothermal activity in the Shihuiyao Rb-Nb-Ta-(Be-Li) deposit, Inner Mongolia, NE China. *Ore Geol. Rev.* **2022**, *150*, 105149. [CrossRef]
59. Kaeter, D.; Barros, R.; Menuge, J.F.; Chew, D.M. The magmatic–hydrothermal transition in rare-element pegmatites from southeast Ireland: LA-ICP-MS chemical mapping of muscovite and columbite–tantalite. *Geochim. Cosmochim. AC* **2018**, *240*, 98–130. [CrossRef]
60. Madayipu, N.; Li, H.; Algeo, T.J.; Muhammad Elatikpo, S.; N'Nahano Heritier, R.; Zhou, H.; Zheng, H.; Wu, Q. Long-lived Nb-Ta mineralization in Mufushan, NE Hunan, South China: Geological, geochemical, and geochronological constraints. *Geosci. Front.* **2023**, *14*, 101491. [CrossRef]
61. Wu, M.; Samson, I.M.; Zhang, D. Textural features and chemical evolution in Ta-Nb oxides: Implications for Deuteric rare-metal mineralization in the Yichun granite-marginal pegmatite, Southeastern China. *Econ. Geol.* **2018**, *113*, 937–960. [CrossRef]
62. Borodulin, G.P.; Chevychelov, V.Y.; Zaraysky, G.P. Experimental study of partitioning of tantalum, niobium, manganese, and fluorine between aqueous fluoride fluid and granitic and alkaline melts. *Dokl. Earth Sci.* **2009**, *427*, 868–873. [CrossRef]
63. Chevychelov, V.; Zaraisky, G.P.; Borisovskiy, S.; Borkov, D.A. Effect of melt composition and temperature on the partitioning of Ta, Nb, Mn, and F between granitic (alkaline) melt and fluorine-bearing aqueous fluid: Fractionation of Ta and Nb and conditions of ore formation in rare-metal granites. *Petrol. C/C Petrol.* **2005**, *13*, 305–321.
64. Zaraisky, G.P.; Korzhinskaya, V.; Kotova, N. Experimental studies of Ta_2O_5 and columbite–tantalite solubility in fluoride solutions from 300 to 550 °C and 50 to 100 MPa. *Miner. Petrol.* **2010**, *99*, 287–300. [CrossRef]
65. Thomas, R.; Davidson, P. Revisiting complete miscibility between silicate melts and hydrous fluids, and the extreme enrichment of some elements in the supercritical state–Consequences for the formation of pegmatites and ore deposits. *Ore Geol. Rev.* **2016**, *72*, 1088–1101. [CrossRef]
66. Thomas, V.G.; Smirnov, S.Z.; Kozmenko, O.A.; Drebushchak, V.A.; Kamenetsky, V.S. Formation and properties of hydrosilicate liquids in the systems Na_2O-Al_2O_3-SiO_2-H_2O and granite-Na_2O-SiO_2-H_2O at 600 °C and 1.5 kbar. *Petrol. C/C Petrol.* **2014**, *22*, 293–309. [CrossRef]
67. Ballouard, C.; Elburg, M.A.; Tappe, S.; Reinke, C.; Ueckermann, H.; Doggart, S. Magmatic-hydrothermal evolution of rare metal pegmatites from the Mesoproterozoic Orange River pegmatite belt (Namaqualand, South Africa). *Ore Geol. Rev.* **2020**, *116*, 103252. [CrossRef]
68. Kaeter, D.; Barros, R.; Menuge, J.F. Metasomatic high field strength element, tin, and base metal enrichment processes in lithium pegmatites from Southeast Ireland. *Econ. Geol.* **2020**, *116*, 169–198. [CrossRef]
69. Zhao, Z.; Yang, X.; Lu, S.; Lu, Y.; Sun, C.; Chen, S.; Zhang, Z.; Ibrahim Bute, S.; Zhao, L. Genesis of late cretaceous granite and its related Nb–Ta–W mineralization in Shangbao, Nanling Range: Insights from geochemistry of whole-rock and Nb–Ta minerals. *Ore Geol. Rev.* **2021**, *131*, 103975. [CrossRef]
70. Smirnov, S.Z.; Thomas, V.G.; Kamenetsky, V.S.; Kozmenko, O.A.; Large, R.R. Hydrosilicate liquids in the system Na_2O-SiO_2-H_2O with NaF, NaCl and Ta: Evaluation of their role in ore and mineral formation at high T and P. *Petrol. C/C Petrol.* **2012**, *20*, 271–285. [CrossRef]
71. Lahti, S.I. Zoning in columbite-tantalite crystals from the granitic pegmatites of the Eräjärvi area, southern Finland. *Geochim. Cosmochim. AC* **1987**, *51*, 509–517. [CrossRef]
72. Neiva, A.M.R.; Gomes, C.L.; Silva, P.B. Two generations of zoned crystals of columbite-group minerals from granitic aplite–pegmatite in the Gouveia area, central Portugal. *Eur. J. Miner.* **2015**, *27*, 771–782. [CrossRef]
73. Guastoni, A.; Pennacchioni, G.; Pozzi, G.; Fioretti, A.M.; Walter, J.M. Tertiary pegmatite dikes of the central alps. *Can. J. Miner. Petrol.* **2014**, *52*, 191–219. [CrossRef]
74. Chládek, Š.; Uher, P.; Novák, M. Compositional and textural variations of columbite-group minerals from beryl-columbite pegmatites in the Maršíkov District, Bohemian Massif, Czech Republic: Magmatic versus hydrothermal evolution. *Can. J. Miner. Petrol.* **2020**, *58*, 767–783. [CrossRef]
75. Victor, V.A.; Yu, A.S. Efficiency of Difference Frequency Generation with ZnGeP2. In *Laser Optics' 98: Gas, Liquid, and Free-Electron Lasers*; SPIE: Bellingham, WA, USA, 1999; pp. 145–150.
76. Van Lichtervelde, M.; Holtz, F.; Melcher, F. The effect of disequilibrium crystallization on Nb-Ta fractionation in pegmatites: Constraints from crystallization experiments of tantalite-tapiolite. *Am. Miner.* **2018**, *103*, 1401–1416. [CrossRef]

77. Legros, H.; Mercadier, J.; Villeneuve, J.; Romer, R.L.; Deloule, E.; Van Lichtervelde, M.; Dewaele, S.; Lach, P.; Che, X.D.; Wang, R.C.; et al. U-Pb isotopic dating of columbite-tantalite minerals: Development of reference materials and in situ applications by ion microprobe. *Chem. Geol.* **2019**, *512*, 69–84. [CrossRef]
78. Che, X.D.; Wu, F.Y.; Wang, R.C.; Gerdes, A.; Ji, W.Q.; Zhao, Z.H.; Yang, J.H.; Zhu, Z.Y. In situ U-Pb isotopic dating of columbite-tantalite by LA-ICP-MS. *Ore Geol. Rev.* **2015**, *65*, 979–989. [CrossRef]
79. Smith, S.R.; Foster, G.L.; Romer, R.L.; Tindle, A.G.; Kelley, S.P.; Noble, S.R.; Horstwood, M.; Breaks, F.W. U-Pb columbite-tantalite chronology of rare-element pegmatites using TIMS and Laser Ablation-Multi Collector-ICP-MS. *Contrib. Miner. Petr.* **2004**, *147*, 549–564. [CrossRef]
80. Sun, X.; Zhu, X.; Tang, H.; Zhang, Q.; Luo, T.; Han, T. Protolith reconstruction and geochemical study on the wall rocks of Anshan BIFs, Northeast China: Implications for the provenance and tectonic setting. *J. Geochem. Explor.* **2014**, *136*, 65–75. [CrossRef]
81. Simmons, W.B.S.; Webber, K.L. Pegmatite genesis: State of the art. *Eur. J. Miner.* **2008**, *20*, 421–438. [CrossRef]
82. Li, P.; Li, J.; Liu, Q.; Wang, D.; Jiang, P.; Tan, H. The first LCT-type mineralized pegmatite in China: Discovery and significance of Yanlingguan spodumene pegmatite in central Shandong. *ACTA Petrol. Sin.* **2024**, *40*, 2621–2637. [CrossRef]
83. Yao, Y.; Li, L.; Fu, J.; Li, H.; Guo, R.; Liu, J.; Wang, Q. Geochronological constraints on early Precambrian granitic pegmatite type Nb-Ta mineralization of the Lijiapuzi deposit in North China craton. *Geol. Bull. China* **2023**, *42*, 1047–1049.
84. Liu, J.; Fu, J.; Yao, Y.; Guo, R.; Wei, C.; Xu, S. Two Nb-Ta mineralization events coeval with the metallogeny of Gongchangling iron ores in the North China Craton: Constraints from geochronology of the columbite-group minerals. *Ore Geol. Rev.* **2025**, *186*, 106842. [CrossRef]
85. Wan, Y.; Liu, D.; Wang, W.; Song, T.; Kröner, A.; Dong, C.; Zhou, H.; Yin, X. Provenance of Meso- to Neoproterozoic cover sediments at the Ming Tombs, Beijing, North China Craton: An integrated study of U–Pb dating and Hf isotopic measurement of detrital zircons and whole-rock geochemistry. *Gondwana Res.* **2011**, *20*, 219–242. [CrossRef]
86. Thomas, R.; Davidson, P.; Beurlen, H. The competing models for the origin and internal evolution of granitic pegmatites in the light of melt and fluid inclusion research. *Miner. Petrol.* **2012**, *106*, 55–73. [CrossRef]
87. Fiege, A.; Simon, A.; Linsler, S.A.; Bartels, A.; Linnen, R.L. Experimental constraints on the effect of phosphorous and boron on Nb and Ta ore formation. *Ore Geol. Rev.* **2018**, *94*, 383–395. [CrossRef]
88. Bartels, A.; Holtz, F.; Linnen, R.L. Solubility of manganotantalite and manganocolumbite in pegmatitic melts. *Am. Miner.* **2010**, *95*, 537–544. [CrossRef]
89. McCauley, A.; Bradley, D.C. The global age distribution of granitic pegmatites. *Can. J. Miner. Petrol.* **2014**, *52*, 183–190. [CrossRef]

Disclaimer/Publisher's Note: The statements, opinions and data contained in all publications are solely those of the individual author(s) and contributor(s) and not of MDPI and/or the editor(s). MDPI and/or the editor(s) disclaim responsibility for any injury to people or property resulting from any ideas, methods, instructions or products referred to in the content.